

## MATHEMATICAL MODELING OF A TWO SPOOL FLOW CONTROL SERVOVALVE USING A PRESSURE CONTROL PILOT<sup>1</sup>

Randy T. Anderson<sup>2</sup> and Perry Y. Li<sup>3</sup>  
Department of Mechanical Engineering,  
University of Minnesota  
111 Church St. SE,  
Minneapolis, MN 55455-0111

### ABSTRACT

A nonlinear dynamic model for an unconventional, commercially available electrohydraulic flow control servovalve is presented. The valve is a two-stage valve and differs from the conventional servovalve in that it does not require a feedback wire and ball, and the boost stage uses two spools, instead of a single spool, to meter flow into and out of the valve separately. Consequently, the valve is significantly less expensive. The proposed model captures the nonlinear and dynamic effects not present in previous models. The model has been coded in *Simulink* and experimentally validated.

### I. INTRODUCTION

The vast majority of flow control servovalves in existence employ a double flapper nozzle pilot stage and a single spool boost stage. A stiff feedback spring is generally used to provide feedback from the boost stage to the pilot. These types of servovalves tend to be difficult to manufacture and expensive. A less conventional, less costly type of flow control servovalve [SauerKVF, 1997] (Sauer-Danfoss Inc., MN, US Patent 4537220) utilizes a two-spool boost stage and a flapper nozzle pressure control pilot. A feedback wire between the nozzle flapper pilot and the boost stage is not needed, thus simplifying assembly. The two spools in the boost stage are spring loaded and separately meter flow into and out of the valve. The main advantages of the two-spool / pressure control pilot design are 1) ease of manufacturing, 2) lower costs, 3) higher degree of adjustment, and 4) greater safety. Because flow into and out of the valve are metered separately using separate spools, the required machining accuracy of the land lengths and of the metering edges are significantly reduced. The shorter bore lengths enable better machining of the metering edges. Electrical displacement transducers are not necessary. Cost advantages stem from the use of modular components, the boost stage housing needs machining only from two sides, and each bore only has one critical axial dimension. The valve can be easily adjusted for different applications since each spool

can be independently positioned. The two-spool design is also potentially safer because unless both spools are jammed open, flow can be shutoff by either spool. Servovalves that utilize the two-spool / pressure control pilot design have a better cost / performance ratio, although they do have lower performance (open loop bandwidth) than their conventional counterparts.

While non-linear dynamic models of the conventional servovalves are well known and are available in the open literature, validated models of similar completeness for a two-spool valve are not available in either academic or industry literature. Anderson (who holds the patent on the design), presented simplified linear models in [Anderson, 1988]. Although the importance of the nonlinearities associated with the valves is recognized, they are not included in these simplified models. In order to predict system performance and stability, and to design control systems in high performance applications, an experimentally validated dynamic model of the valve capable of predicting valve behavior under a wide range of conditions is needed. A mathematical model relating the various physical parameters to performance can also be used to predict and improve the performance in the physical design of the valves. In this paper an experimentally validated physical model of the valve that uses a two-spool / pressure pilot design is presented. The model takes into account nonlinear effects such as flow forces, nonlinear magnetic effects, and chamber fluid compressibility. The model is capable of predicting the dynamic output flow rate when the time courses of electrical current input and work port pressures are given.

The rest of the paper is organized as follows. The basic operation of the valve is given in section II. Models for subsystems are developed next: sections III and IV describe the models for the pilot and the boost stages, the chamber pressure dynamics are given in section V, and the output flow equations are given in section VI. In section VII, simulation issues are discussed. Simulation and experimental results are shown in section VIII. Conclusions are given in section IX. A table of nomenclature appears at the end of the paper.

---

<sup>1</sup> Research performed as part of Mechanical Engineering, Honor Thesis at the University of Minnesota.

<sup>2</sup> Undergraduate student. Email: ande2076@tc.umn.edu

<sup>3</sup> Assistant Professor and Corresponding author. Email: pli@me.umn.edu

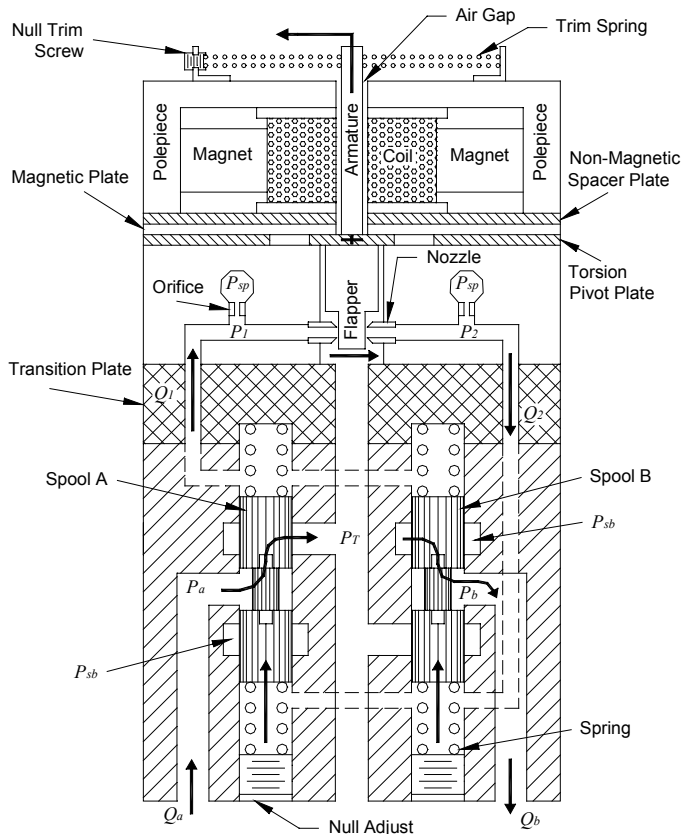


Figure 1, Two Spool Flow Control Servovalve

## II. OPERATION

A schematic of the flow control servovalve using a two-spool, and pressure control pilot design is shown in Fig. 1. It consists of two distinct stages; a pilot and a boost stage, connected together by a simple transition plate. The pilot stage is a pressure control pilot [SauerMCV, 1999], which uses a double nozzle flapper design. The boost stage of the valve consists of two separate spring centered spools which meter flow into and out of the valve separately.

Roughly speaking, the pressure control pilot stage generates a differential pilot pressure proportional to the electrical current input to the electromagnetic torque motor. The differential pilot pressure acts on the two ends of both spools. Since the spools are spring centered, the displacements of the spools are roughly proportional to the differential pilot pressure and inversely proportional to the stiffness of the springs. Flow into and out of the valve are metered by the displacements of the spools. Notice that a feedback wire between the boost stage and the pilot stage is not used in this design. The interconnection between the subsystems of the valve is shown in Fig. 2.

A more detailed discussion of the operation of the valve follows. Note that in Fig. 1, bold arrows correspond to the direction of fluid flow. Suppose that an electrical current is the input to the coil of the torque motor at the top part of the valve in Fig. 1. The current in the coil, together with the magnetic armature, generates a torque, which in turn rotates the armature and flapper in the counter-clockwise motion about the pivot point (where the armature and the flapper intersect). As the flapper displaces to the right (left), the nozzle opening on the

right (left) decreases and the opening on the left (right) increases. This in turn raises  $P_2$  and lowers  $P_1$  (or vice versa). The differential pressure  $P_2 - P_1$ , therefore, has the effect of restoring the flapper to its neutral position. Since the magnetic circuit in the torque motor is usually sized to exactly cancel out the mechanical stiffness of the pivot [Anderson, 1988], the pivot has a small effective stiffness. Because of this, the torque generated in the torque motor is balanced predominantly by the differential pressure  $P_2 - P_1$ . Consequently, in the steady state, the differential pressure should be roughly proportional to the input current.

The pilot pressures,  $P_1$  and  $P_2$ , act on the two ends of each spool. A positive (negative) differential pressure  $P_2 - P_1$  causes both spools to move in the upward (downward) direction. As spools A and B move upward (downward), hydraulic oil is ported from the supply to port B (A) on one side, and from port A (B) into the tank on the other, creating flows  $Q_a$  and  $Q_b$  respectively. As the spools displace, flows  $Q_1$  to and  $Q_2$  from the pilot stage are also created.

The regulation of the spool displacements (hence the flow rate) is achieved in two ways. Primarily, displacements of the spools are resisted by the compression of the springs. Thus, in the steady state, the displacement of each spool would be proportional to the differential pilot pressure and inversely proportional to the spring stiffness. Secondly, the displaced fluid volume above and below the spools also tend to reduce the differential pressure. Therefore, the upward (downward) spool displacement and velocity tend to decrease  $P_2 - P_1$ . These effects in turn affect the flapper displacement and the differential pilot pressure. If the system is stable, the spool will reach an equilibrium displacement.

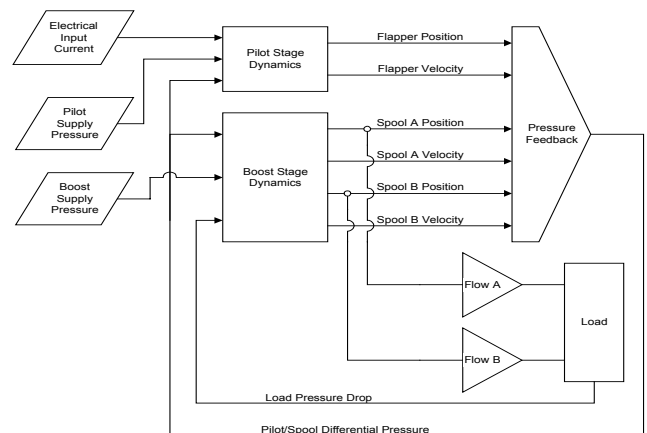


Figure 2. Signal flow diagram of the valve

## III. PILOT STAGE DYNAMICS

The physical model for the pilot stage will be derived in this section. The free body diagram of the armature-flapper assembly is shown in Fig. 3. The armature-flapper is subjected to the magnetic force,  $F_g$ , applied at the top air gap, the trim spring force,  $F_k$ , at the end of the armature, the damping moment on the armature (created as the armature moves in the silicon oil that fills the area above the flapper), the moment due to the pivot stiffness, and the nozzle flow forces,  $F_f$ .

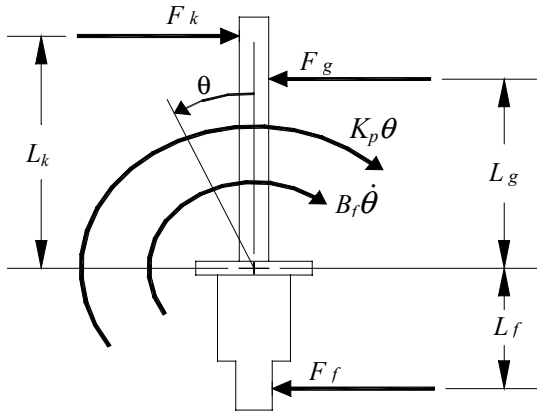


Fig. 3. Free body diagram of the armature-flapper

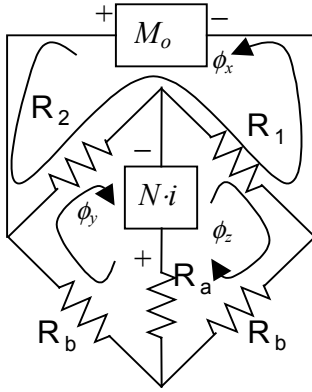


Figure 4. Armature magnetic circuit

The magnetic force,  $F_g$ , is found by analyzing the magnetic circuit shown in Fig. 4.  $R_a$  is the reluctance due to the lower air gap between the magnetic plate and the armature while  $R_b$  is the reluctance between the polepieces and the magnetic plate.  $R_1$  and  $R_2$  correspond to the reluctances at the two top air gaps between the polepieces and the armature. They are functions of the linear armature displacement,  $x_g = L_g \theta$ .  $R_a$ ,  $R_b$ ,  $R_1$ , and  $R_2$  are given by:

$$R_a = \frac{G_a}{\mu_{\text{silicon}} A_a}, \quad R_b = \frac{G_b}{\mu_{\text{plate}} A_b} \quad (1)$$

$$R_1 = \frac{G_g + x_g}{\mu_{\text{silicon}} A_g}, \quad R_2 = \frac{G_g - x_g}{\mu_{\text{silicon}} A_g} \quad (2)$$

In Fig. 4,  $N \cdot i$  is the magnetomotive force (MMF) due to an input current  $i$  flowing in the  $N$ -turn coil.  $M_o$  is MMF of the permanent magnet. The magnetic fluxes  $\phi_x$ ,  $\phi_y$ ,  $\phi_z$  satisfy the following magnetic flux equations:

$$M_o = R_1(\phi_x + \phi_z) + R_2(\phi_x + \phi_y) \quad (3)$$

$$Ni = R_2(\phi_y + \phi_x) + R_b(\phi_y) + R_a(\phi_y - \phi_z) \quad (4)$$

$$-Ni = R_1(\phi_z + \phi_x) + R_b(\phi_z) + R_a(\phi_z - \phi_y) \quad (5)$$

which can be used to solve for the fluxes,  $\phi_x$ ,  $\phi_y$ ,  $\phi_z$ . The magnetic force is given by [Merritt, 1967]:

$$F_g = 4.42 \times 10^{-8} \left( \frac{\phi_1^2 - \phi_2^2}{\mu_o A_g} \right) \text{ lb.} \quad (6)$$

where fluxes  $\phi_1$  and  $\phi_2$  are the magnetic fluxes in the air gaps given by  $\phi_1 = \phi_x + \phi_y$ , and  $\phi_2 = \phi_x + \phi_z$ . Substituting Eqs. (1)-(5) into Eq. (6), we obtain:

$$F_g = \alpha_0 \frac{\alpha_1 \cdot i + \alpha_2 \cdot (i^2 x_g) + \alpha_3 \cdot (i x_g^2) + \alpha_4 \cdot x_g}{(\beta_1 - \beta_2 x_g^2)^2} \quad (7)$$

where

$$\alpha_0 = 4.42 \times 10^{-8} \mu_o \mu_{\text{silicon}}^2 \mu_{\text{r-plate}} A_a A_b A_g$$

$$\alpha_1 = 2 \mu_{\text{r-plate}} G_g N M_o (2 A_b G_a A_g + A_a A_b G_g) + 2 \mu_{\text{r-silicon}} A_g G_g A_a G_b N M_o$$

$$\alpha_2 = 4 \mu_{\text{r-plate}} A_a A_b G_g N^2$$

$$\alpha_3 = 2 \mu_{\text{r-plate}} A_a A_b N M_o$$

$$\alpha_4 = \mu_{\text{r-plate}} A_a A_b G_g M_o^2 + \mu_{\text{r-silicon}} A_a A_g G_b M_o^2 + 2 \mu_{\text{r-plate}} A_b A_g G_a M_o^2$$

$$\beta_1 = \mu_{\text{r-plate}} A_a A_b G_g^2 + \mu_{\text{r-silicon}} A_a A_g G_b G_g + 2 \mu_{\text{r-plate}} A_b A_g G_a G_g$$

$$\beta_2 = \mu_{\text{r-plate}} A_a A_b$$

The next term to determine is the trim spring force  $F_k$ . Because there are two trim springs with spring constant  $K_k$ , the total trim spring force is:

$$F_k = 2K_k x_k = 2K_k (L_k \theta). \quad (8)$$

Nozzle forces on the flapper are well studied and are given by [Merritt, 1967]:

$$F_f = (P_2 - P_1) A_n + 4\pi C_{df}^2 [(x_{f0} - x_f)^2 P_2 - (x_{f0} + x_f)^2 P_1] \quad (9)$$

where the first term corresponds to the static pressure force, and the second term corresponds to the flow forces at the nozzle.

The pivot stiffness of the armature-flapper was found using published torsion equations. The pivot stiffness (in-lbs/rad) for the rectangular shaped pivot is given by [Roark and Young, 1975]:

$$K_p = 2 \frac{h_t w_t^3}{16} \left[ \frac{16}{3} - 3.36 \frac{w_t}{h_t} \left( 1 - \frac{w_t^4}{12 h_t^4} \right) \right] \frac{G}{L_t} \quad \text{for } w_t < h_t. \quad (10)$$

Summing moment about the pivot, applying Newton's second law, and apply the relationships between the angular armature displacements and the linear armature and flapper displacements:

$$x_f = L_f \theta, \quad x_g = L_g \theta = \frac{L_g}{L_f} x_f \quad (11)$$

we obtain:

$$J \ddot{\theta} = \frac{J}{L_f^2} \ddot{x}_f = F_g L_g - F_k L_k - F_f L_f - K_p \theta - B_f \dot{\theta} \quad (12)$$

where  $J$  is the moment of inertia of the armature-flapper, and  $B_f$  is the angular damping coefficient.

Using Eq. (11), Eq. (12) can be written in terms of  $x_f, \dot{x}_f$ .

This way, we obtain a second order model for the pilot stage in the form of

$$\ddot{x}_f = f_{pilot}(x_f, \dot{x}_f, i, P_1, P_2) \quad (18)$$

where  $x_f, \dot{x}_f$  are the states, and  $i, P_1, P_2$  are the inputs.

#### IV. BOOST STAGE DYNAMICS

The model for the boost stage are developed next. We need to derive the dynamic equations that describe the two spools. We will analyze spool A in Fig. 5 in detail. The equations for spool B can be similarly derived. We assume the spools are designed to be critically centered. In Fig. 5, the spool is subjected to differential pilot pressure, a force due to the centering spring, viscous friction and flow forces. Equating forces on the spool yields the following:

$$M_s \ddot{x}_s = (P_2 - P_1)A_s - 2K_s x_s - F_V - F_F \quad (19)$$

where RHS are forces due to the differential pressure,  $F_F$  is the due to the centering spring, and  $F_V$  is the viscous damping force.  $K_s$  is the stiffness of the centering spring.

Assuming a perfectly centered spool in a bore [Merritt, 1967] the viscous damping force is:

$$F_V = \frac{\pi D_s L_s \mu}{C_r} \dot{x}_s \quad (20)$$

The fluid flow forces  $F_F$  that the spool encounter are sometimes called Bernoulli forces which arise due to the dynamics of the fluid flow. There are two types of flow forces: steady state flow forces and transient flow forces. Steady state flow forces are due to the angle of the Vena Contracta as the fluid is metered into or out of the valve. They depend on the flow rate and hence the spool displacement. Transient flow forces, on the other hand, are the reactive forces associated with the acceleration of the fluid in the chamber. Thus, they are dependent on the rate of change of flow and the spool velocity. The signs of the steady state and transient components depend on the spool displacements, velocities and on whether the spool is metering flow into or out of the valve. Following [Merritt, 1967], the fluid flow forces on spool A are given by:

$$F_F = \begin{cases} C_{dj} C_v w (P_a - P_T) \cos(\theta_j) \cdot x_a \\ \quad + L_p C_{dj} w \sqrt{2\rho(P_{sb} - P_a)} \cdot \dot{x}_a & x_a \geq 0 \\ C_{dj} C_v w (P_{sb} - P_a) \cos(\theta_j) \cdot x_a \\ \quad - L_p C_{dj} w \sqrt{2\rho(P_{sb} - P_a)} \cdot \dot{x}_a & x_a < 0 \end{cases} \quad (21)$$

where the first term corresponds to the steady state flow force, and the second term corresponds to the transient flow force. In Eq. (21), the effect of clearance can be taken into account by

replacing  $x_a$  by  $\text{sign}(x_a) \sqrt{x_a^2 + C_r^2}$  in the first term. Notice that regardless of the sign of  $x_a$ , the steady state flow force is always restoring and acts like a spring to close the valve. On the other hand, the transient flow force is proportional to the spool velocity, acts like a positive stabilizing damping, when  $x_a \geq 0$  (when flow is being metered out of the valve). It acts like a negative, unstable damping when  $x_a < 0$  (flow is being metered into the valve). Transient flow forces therefore can be a source of valve instability. A recent investigation of the benefits of exploiting the instability induced by transient flow force is given in [Krishnaswamy and Li, 2000].

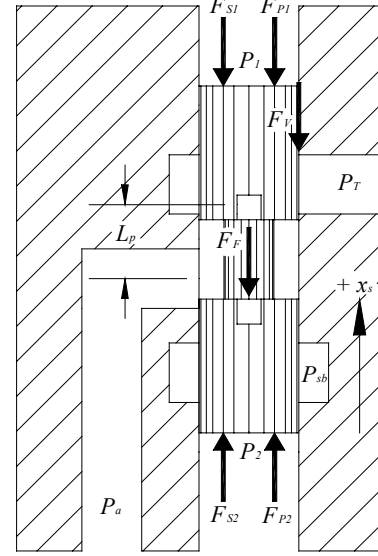


Figure 5. Free Body Diagram for spool A.

In Eq. (21),  $L_p$  is the damping length, which is the length of the fluid column that undergoes acceleration. The transient flow force is therefore proportional to damping length. For the valve being considered,  $L_p$  depends on the spool displacement:

$$L_p = L_{p0} + |x_s/2| \quad (22)$$

where  $L_{p0}$  is the damping length when the spool displacement is zero. The transient flow force can be under-estimated by as much as 10% if  $L_p$  is considered a constant.

In Eq.(21),  $\theta_j$  is the fluid jet angle of the Vena Contracta. It is a nonlinear function of  $x_a/Cr$  [Merritt, 1967].  $\theta_j$  varies from  $69^\circ$  at large spool displacements to  $21^\circ$  at small orifice openings. These differences can cause large deviations in the steady state flow force term ( $\cos(21^\circ)/\cos(69^\circ) = 2.6$ ). To account for this variation, we use a high order polynomial to fit the dependence of  $\theta_j$  on  $x_s/Cr$  to a curve.

Similar to Eq. (21), the downward flow forces for spool B can be equivalently derived:

$$F_F = \begin{cases} C_{dj} C_v w (P_{sb} - P_b) \cos(\theta_j) \cdot x_b \\ \quad - L_p C_{dj} w \sqrt{2\rho(P_{sb} - P_b)} \cdot \dot{x}_b & x_b \geq 0 \\ C_{dj} C_v w (P_b - P_T) \cos(\theta_j) \cdot x_b \\ \quad + L_p C_{dj} w \sqrt{2\rho(P_b - P_T)} \cdot \dot{x}_b & x_b < 0 \end{cases} \quad (23)$$

Substituting Eqs.(20)-(23) into Eq. (19), the dynamics of the two spools are described by two sets of second order dynamic systems, of the form:

$$\ddot{x}_a = f_{sp1}(x_a, \dot{x}_a, P_1, P_2, P_a, P_b) \quad (24)$$

$$\ddot{x}_b = f_{sp2}(x_b, \dot{x}_b, P_1, P_2, P_a, P_b) \quad (25)$$

where the spool displacements and velocities  $x_a$  and  $\dot{x}_a$ , and  $x_b$  and  $\dot{x}_b$ , are the states, and the chamber pressures,  $P_1$ ,  $P_2$  and work port pressures  $P_a$ ,  $P_b$  are the input. Notice that the work port pressures play only a minor role in the spool dynamics via the flow forces in Eqs. (21), (23).

## V. CHAMBER PRESSURE DYNAMICS

The pilot pressures  $P_1$  and  $P_2$  are needed as inputs to both the pilot Eq.(18), and the boost stage Eqs.(24)-(25) dynamics. These are determined by the compressibility of the fluid in the chamber between the pilot stage and the boost stage.

To determine the pressures,  $P_1$  and  $P_2$ , we use the basic hydraulic compressibility equations

$$\dot{P}_1 = (\dot{Q}_1 - \dot{V}_1) \frac{\beta}{V_1}, \quad \dot{P}_2 = (\dot{Q}_2 - \dot{V}_2) \frac{\beta}{V_2} \quad (26)$$

The volume  $V_1$  in Eq.(26) is the fluid volume between the top of the spools and the left flapper face, and  $V_2$  corresponds to the chamber volume between the bottoms of the spools and the right flapper face.  $\dot{Q}_1$  and  $\dot{Q}_2$  are the flow into the chamber. Recall that an upward spool displacement is defined to be positive. The chamber volumes are therefore given by:

$$V_1 = V_{1o} - A_s x_a - A_s x_b, \quad V_2 = V_{2o} + A_s x_a + A_s x_b \quad (27)$$

$V_{1o}$  and  $V_{2o}$  are the initial fluid volumes in all the lines and chambers between spool ends and the flapper at null. Differentiating Eq.(27), we have

$$\dot{V}_1 = -A_s \dot{x}_a - A_s \dot{x}_b, \quad \dot{V}_2 = A_s \dot{x}_a + A_s \dot{x}_b. \quad (28)$$

Flows  $\dot{Q}_1$  and  $\dot{Q}_2$  into the chamber comprise of the flow from the pilot supply orifice, leakage past the nozzle, and leakage past the spools. Combining these three contributions, we get:

$$\dot{Q}_1 = C_{do} A_o \sqrt{\frac{2}{\rho} (P_{sp} - P_1)} - C_{df} \pi D_n (x_{fo} + x_f) \sqrt{\frac{2}{\rho} (P_1)} - \frac{\pi D_b C_r^3 P_1}{12 \mu (L_{lo} + x_a)} + \frac{\pi D_b C_r^3 (P_{sb} - P_1)}{12 \mu (L_{lo} + x_b)} \quad (29)$$

$$\dot{Q}_2 = C_{do} A_o \sqrt{\frac{2}{\rho} (P_{sp} - P_2)} - C_{df} \pi D_n (x_{fo} - x_f) \sqrt{\frac{2}{\rho} (P_2)} + \frac{\pi D_b C_r^3 (P_{sb} - P_2)}{12 \mu (L_{lo} - x_a)} - \frac{\pi D_b C_r^3 (P_2)}{12 \mu (L_{lo} - x_b)} \quad (30)$$

where the leakages are modeled to be laminar flows in an annulus between a annular shaft and a concentric cylinder.

Substituting Eqs.(27)-(30) into Eq.(26), Eq. (26) becomes the dynamic models for each fluid chamber, with  $P_1$  and  $P_2$  as the states, and the spool displacements and velocities as the input.  $P_1$  and  $P_2$  can be used as the input to the pilot stage dynamics (18) and the boost stage dynamics (24)-(25).

At this point, all of the necessary differential equations have been developed to describe the pilot stage, spool A, spool B, and the chamber pressures,  $P_1$  and  $P_2$ . There are, in total, eight (8) state variables. Next, we describe how the output flows at the work ports are related to the states of the valve.

## VI. FLOW EQUATIONS

As the spools in the boost stage move, flow is either metered into or out of the valve through the orifice. In addition to the orifice flow, the total flow at the work ports is also contributed by leakage flows through the spool-bore clearance (see Fig. 6). Leakage is again modeled by laminar flow in an annulus between an annular shaft and a concentric cylinder.

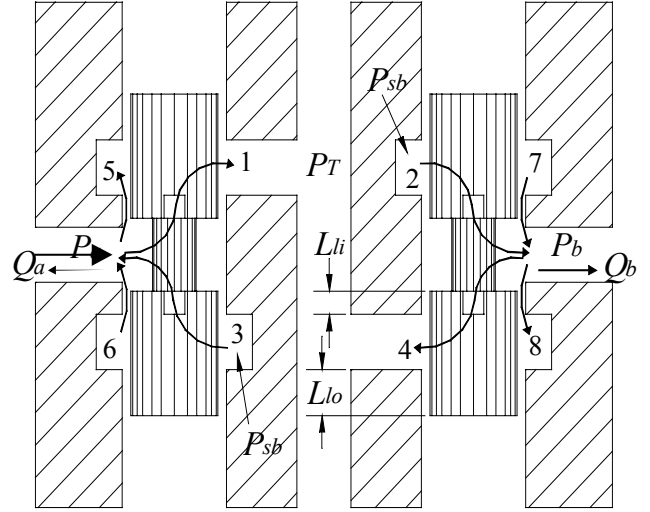


Figure 6, Flow Elements

For spool A in Fig. 6, when the spool displacement is positive, the flow paths 1, 5, 6 are active; and for negative displacements, flow paths 3, 5, 6 are active. Therefore,

$$\dot{Q}_a = \begin{cases} C_d w x_a \sqrt{\frac{2(P_a - P_T)}{\rho}} + \frac{\pi D_b C_r^3 (P_a - P_T)}{12 \mu (L_{li} - x_a)} - \frac{\pi D_b C_r^3 (P_{sb} - P_a)}{12 \mu (L_{li} + x_a)} & x_a \geq 0 \\ C_d w x_a \sqrt{\frac{2(P_{sb} - P_a)}{\rho}} + \frac{\pi D_b C_r^3 (P_a - P_T)}{12 \mu (L_{li} - x_a)} - \frac{\pi D_b C_r^3 (P_{sb} - P_a)}{12 \mu (L_{li} + x_a)} & x_a < 0 \end{cases} \quad (31)$$

The first term in each of the two cases correspond to the orifice flow, and the other terms correspond to the leakage. Notice that when  $x_a < 0$ , the orifice flow is negative.

For spool B and for positive spool displacement, the flow paths 2, 7, 8 are active in Fig. 6. When the spool displacement is negative, flow paths 4, 7, 8 are active. Hence,

$$Q_b = \begin{cases} C_d w x_b \sqrt{\frac{2(P_{sb} - P_b)}{\rho} + \frac{\pi D_b C_r^3 (P_{sb} - P_b)}{12\mu(L_{li} - x_b)} - \frac{\pi D_b C_r^3 (P_b - P_T)}{12\mu(L_{li} + x_b)}} & x_b \geq 0 \\ C_d w x_b \sqrt{\frac{2(P_b - P_T)}{\rho} + \frac{\pi D_b C_r^3 (P_{sb} - P_b)}{12\mu(L_{li} - x_b)} - \frac{\pi D_b C_r^3 (P_b - P_T)}{12\mu(L_{li} + x_b)}} & x_b < 0 \end{cases} \quad (32)$$

Notice that Eqs. (30)-(31) have been derived with the assumption that  $0 = P_T \leq P_a, P_b \leq P_{sb}$ . They define the flow that enters the valve through work port A, and the flow that leaves the valve through work port B. Beyond the work ports, there are other losses, including channels in the body, lines, fittings, etc. These must be taken into consideration when calculating the flow in a complete system.

## VII. MATLAB/SIMULINK MODEL

The dynamic models for the pilot stage, Eq.(18), boost stage, Eqs.(24)-(25), and the chamber pressure dynamics Eq.(26) can be connected to each other, and to a hydraulic device, such as in Fig. 2, into a simulation model. The combined model will be capable of predicting the flows  $Q_a, Q_b$  into and out of the work ports, given the input of the time trajectories of the input current,  $i$ , the two work port pressures  $P_a, P_b$ .

In order to simplify the testing procedure, it will be convenient to assume that  $Q_a = Q_b$ , i.e. the valve is connected to volume conserving devices (such as a double ended cylinder or a hydraulic motor). This allows us to specify only the load-pressure,  $P_L := P_b - P_a$ , instead of specifying  $P_a$  and  $P_b$  independently. To this end, we calculate  $P_a$  and  $P_b$  given  $P_L$ . Equating the output flows in Eqs.(31)-(32), and neglecting the leakage flows, we obtain for usual combinations of  $x_a, x_b$ :

$$x_a, x_b \geq 0: P_a = \frac{x_b^2 (P_{sb} - P_L)}{x_a^2 + x_b^2}, P_b = \frac{x_b^2 P_{sb} + x_a^2 P_L}{x_a^2 + x_b^2};$$

$$x_a, x_b < 0: P_a = \frac{x_a^2 P_{sb} - x_b^2 P_L}{x_a^2 + x_b^2}, P_b = \frac{x_a^2 (P_{sb} + P_L)}{x_a^2 + x_b^2}. \quad (33)$$

When  $x_a, x_b$  are of different signs (which generally do not occur), it would be necessary to assume that  $P_a$  or  $P_b$  is either above  $P_{sb}$  or below  $P_T$ . In this situation, the simplifying assumption that  $Q_a = Q_b$  is probably not valid.

With the simplification that  $Q_a = Q_b$ , the *Matlab / Simulink* model is shown in Fig. 7. The model of each of the subsystems (pilot, boost, pressure chambers) and the output flow equations, have been developed in a complete manner without resorting to empirical simplifications. All the parameters of the models, except for the pilot damping coefficient  $B_f$  are estimated from the component characteristics and the physical valve design.  $B_f$  is determined to match the experimental results. The subsystems were coded in S-Function blocks instead of using a completely graphical representation

because of the model complexities. The input/output variables of each subsystem and their connections are shown in Fig. 7.

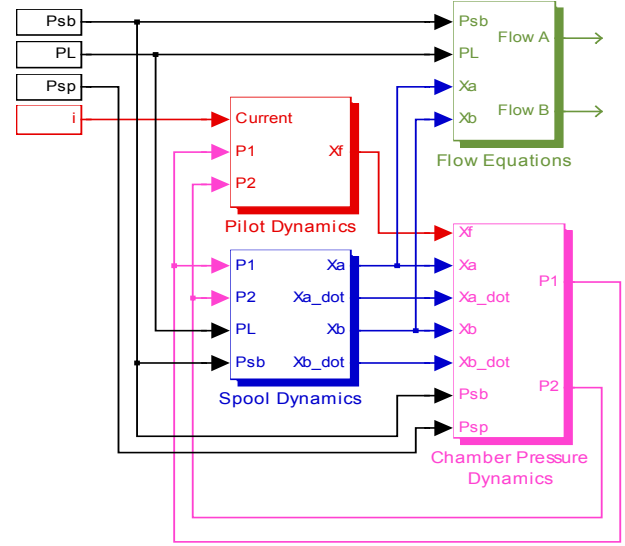


Figure 7, Simulink Block Diagram

Notice that the S-Function for the pilot stage receives as inputs, the input current ( $i$ ) and the pilot pressure on the flapper ( $P_1, P_2$ ). Each of the spool S-Functions also receive the same pilot pressure ( $P_1, P_2$ ), work port pressure drop ( $P_L$ ), and boost supply pressure ( $P_{sb}$ ).  $P_a$  and  $P_b$  are calculated in the subsystems given the load pressure  $P_L$  and spool displacements.

Notice in Fig. 7 that the operation of the two-spool / pressure control pilot valve utilizes two feedback loops in its design. The principal feedback loop consists of the pilot stage, and the pressure dynamics. This feedback loop controls the differential pilot pressure. The secondary loop involves the boost stage and the pressure dynamics. While the chamber pressure dynamics affect the boost stage significantly, the effect of boost stage on the chamber pressure is not as significant.

## VIII. SIMULATION AND EXPERIMENTAL RESULTS

To validate the model, the Simulink model is compared with experimental results under similar conditions. The experimental setup consists of the two-spool flow control valve connected to a flow motor via a set of butterfly valves. The speed of the flow motor provides the flow measurement. The current input to the valve can be adjusted continuously using a computer. The butterfly valves can be adjusted offline to simulate different load pressures  $P_L$ . The pilot pressures,  $P_1$  and  $P_2$ , as well as the work port pressures are measured.

### Steady State Response

The steady state  $Q$  vs.  $i$  (at no load) and  $Q$  vs.  $P_L$  (at various current  $i$ 's) plots are used to assess the steady state response (Fig. 8). For the  $Q$  vs.  $i$  plot, the current was varied between 0-40 mA (100%) sinusoidally at 0.25Hz. From Fig. 8, we see that simulation and experiments show excellent match: the  $Q$  vs.  $i$  relationship is linear and show a slight hysteresis.

For the  $Q$  vs.  $P_L$  plot, the load pressure was varied between 0-3075 psi ( $P_{sb}$ ) slowly by hand. The plot shows the familiar square root power relationship, as expected from (31) and (32). Notice that Fig. 8 includes results from multiple experiments.

The simulation results fall within the uncertainty of the measurements.

### Time Response

To evaluate the time response of the valve, various step current inputs at near zero load pressure drop were applied to the model and to the experimental setup. Limitation of the current driver makes a slight overshoot in the input current, and short rise time (8 ms) unavoidable. The same non-ideal current “step” was used in simulation. The near “step” responses are shown in Fig. 9. The experimental and simulated responses are very similar; both showing a rise-time of approximately 20 to 30 msec with the experimental setup perhaps slightly faster. From the plots notice that the experimental data has a slight time delay of 4 msec relative to the simulation that could be caused by the fact that the flow motor used for flow measurement has a finite inertia. Also, the hydraulic lines used in the experiments are spongy which can also cause some overshoot. This is confirmed by a test that was conducted with the valve mounted directly on the flow motor in which the large overshoot disappeared.

### Frequency Response

The frequency response is investigated next. The frequency response (Fig. 10) was obtained by superimposing a 10mA (25%) swept sinusoidal current on a D.C. biased current (20mA – 50%) at a zero load pressure. Experimentally, the frequency is obtained via an FFT analyzer. The bandwidth of the experimental system, determined from the amplitude plot (-3 dB) is approximately 25 Hz with a roll-off of -30 dB/decade; this bandwidth is only slightly slower than expected (manufacturer claims +30 Hz) and can be caused by the flow motor inertia. The bandwidth of the model is slightly lower (20 Hz, a roll-off of -20 dB/decade). The difference in phase responses between the experimental system and the model may be due to time lag / flow measurement dynamics.

## IX. CONCLUSIONS

A mathematical dynamic model of an unconventional flow control servovalve with a two-spool boost stage and a pressure control pilot design has been developed and experimentally validated. The model consists of the interconnection between the pilot stage, the two spools in the boost stage, chamber pressures, and output flow relationships. The model has been implemented using *Matlab/Simulink*. Steady state and step responses show excellent agreements between simulation, experimental results, and manufacturer specifications. Dynamically, the response of the model is comparable except that the bandwidth of is slightly lower than indicated by the experimental system. The phase characteristics are also somewhat different.

Implementing nonlinear dynamic models in *Simulink* using S-Functions is very convenient. A major advantage of the proposed model is that empirical data is not used in deriving the governing physics. Using the model, design changes can be analyzed quickly. The proposed dynamic model will also be useful in the design and analysis of control systems that utilize this valve in higher performance applications.

## ACKNOWLEDGMENTS

The authors thank Sauer-Danfoss Inc., Minneapolis, MN for the use of experimental facilities and Mr. Wayne R. Anderson of Sauer-Danfoss Inc. for helpful discussions.

## REFERENCES

- Anderson, W. R., 1988, *Controlling Electrohydraulic Systems*, Marcel Dekker, NY.
- Krishnaswamy, K. and Li, P. Y., 2000, “On using unstable electrohydraulic for control”. Proceedings of the 2000 American Control Conference.
- Merritt, H. E., 1967, *Hydraulic Control Systems*. John Wiley and Sons.
- Roark, R. J. and Young, W. C., 1975, *Formulas for Stress and Strain*, fifth edition. McGraw-Hill Book Company.
- SauerMCV, 1999 *MCV116 Pressure control pilot valve product description*. Sauer-Danfoss Inc. BLN-95-9033-1.
- SauerKVF, 1997 *Flow Control Servovalve product description*. Sauer-Danfoss Inc. BLN-95-9061.

## NOMENCLATURE

$A_a, A_b, A_g$	Air gap cross sectional areas
$A_n$	Nozzle area
$A_o$	Supply orifice area
$A_s$	Spool area
$B_f$	Damping coefficient of pilot stage
$C_{df}$	Flapper-nozzle discharge coefficient
$C_{dj}$	Jet discharge coefficient
$C_{do}$	Supply orifice discharge coefficient
$C_r$	Radial clearance between bore and
$C_v$	Velocity coefficient
$D_b$	Bore diameter
$D_n$	Nozzle diameter
$D_n$	Pilot nozzle diameter
$D_o$	Supply orifice diameter
$D_s$	Spool diameter
$F_F$	Flow force on spool
$F_f$	Pressure and flow forces on flapper
$F_g$	Attractive force between magnetized parallel surfaces separated by an air gap
$F_k$	Trim spring force on armature
$F_{p1}, F_{p2}$	Spring forces on spool
$F_{s1}, F_{s2}$	Spring forces on spool
$F_V$	Viscous damping force on spool
$G$	Shear modulus of material
$G_a, G_b, G_g$	Air gap lengths ( $G_g$ is at null) gap
$h_t$	Height of pivot cross section
$i$	Input current
$J$	Mass moment of inertia of armature-flapper assembly
$K_k$	Spring constant of trim springs
$K_p$	Pivot Stiffness of armature-flapper
$K_s$	Spring constant of spool springs
$L_f$	Length from pivot to center of nozzle
$L_g$	Length from pivot to center of top air
$L_{li}$	Initial spool length for inner leakage
$L_{lo}$	Initial spool length for outer leakage
$L_p$	Length between work port and jet
$L_{po}$	Initial length between work port and orifice jet
$L_s$	Total spool length in contact with bore for damping ( $2(L_{li} + L_{lo})$ )
$l_t$	Length of one side of pivot bar

$M_o$	Permanent Magnet mmf
$M_s$	Spool mass
$N$	Number of coil turns orifice
$P_1, P_2$	Pilot Pressures
$P_a$	Pressure of Port A
$P_b$	Pressure of Port B
$P_L$	Pressure drop across the work ports
$P_{sb}$	Supply pressure to boost
$P_{sp}$	Supply pressure to pilot spool
$R_a, R_b$	Fixed reluctances in magnetic circuit
$R_1, R_2$	Variable reluctances in magnetic circuit
$w$	Orifice area gradient
$w_t$	Width of pivot cross section
$x_a$	Spool A position
$x_b$	Spool B position
$x_f$	Flapper to nozzle distance
$x_{fo}$	Flapper to nozzle distance at null
$x_g$	Position of armature at top air gap
$x_s$	Spool position in general
$\beta$	Bulk Modulus of hydraulic oil
$\rho$	Density of hydraulic fluid
$\mu$	Viscosity of hydraulic fluid
$\mu_o$	Permeability of free space
$\mu_{r-plate}$	Relative permeability of non-magnetic spacer plate
$\mu_{r-silicon}$	Relative permeability of air
$\mu_{plate}$	Permeability of non-magnetic spacer plate in magnetic circuit ( $\mu_{silicon} = \mu_{r-silicon} \mu_o$ )
$\mu_{silicon}$	Permeability of silicon in magnetic circuit ( $\mu_{silicon} = \mu_{r-silicon} \mu_o$ )
$\theta$	Rotation angle of flapper-armature
$\theta_j$	Jet angle of fluid at spool orifice

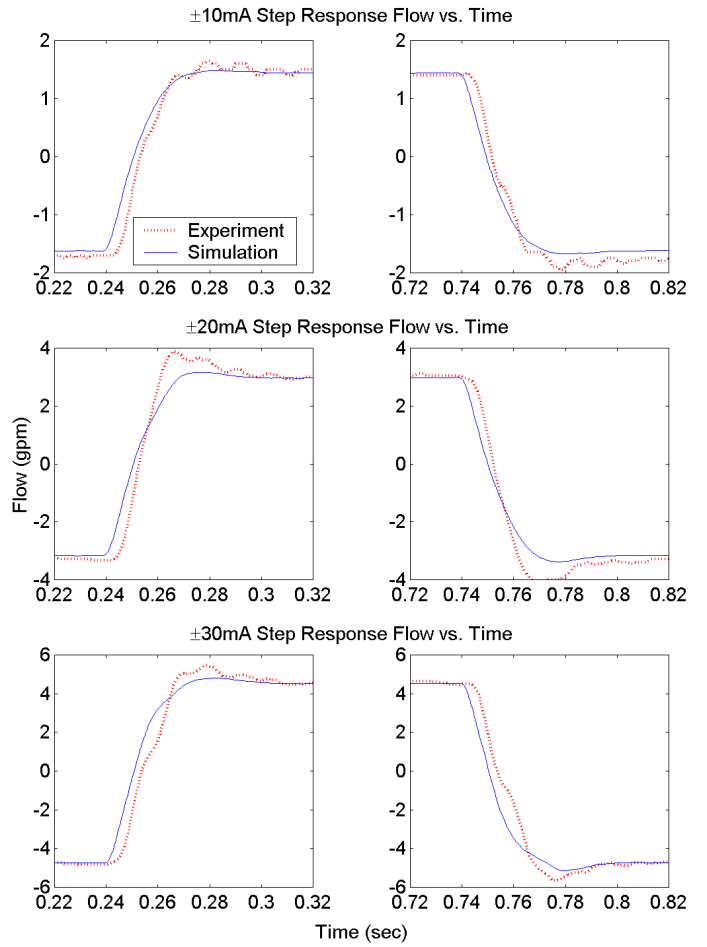


Figure 9, Step Response Curves

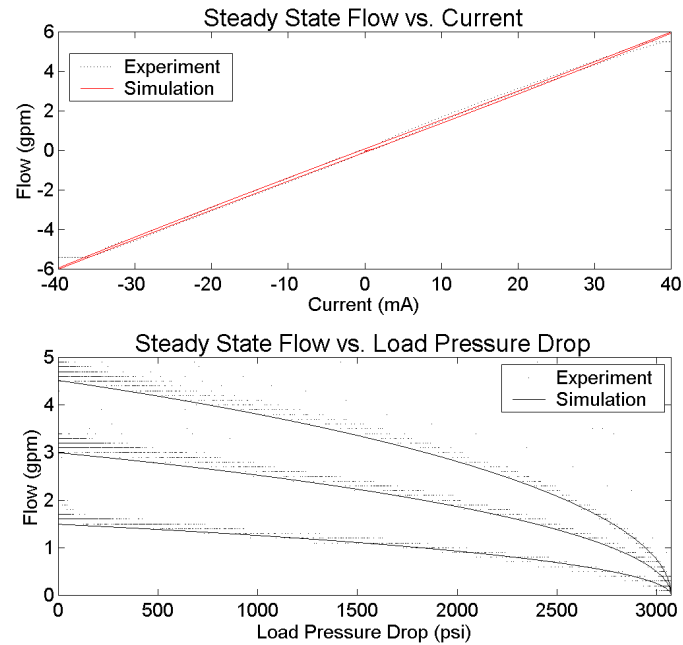


Figure 8, Steady State Response Curves

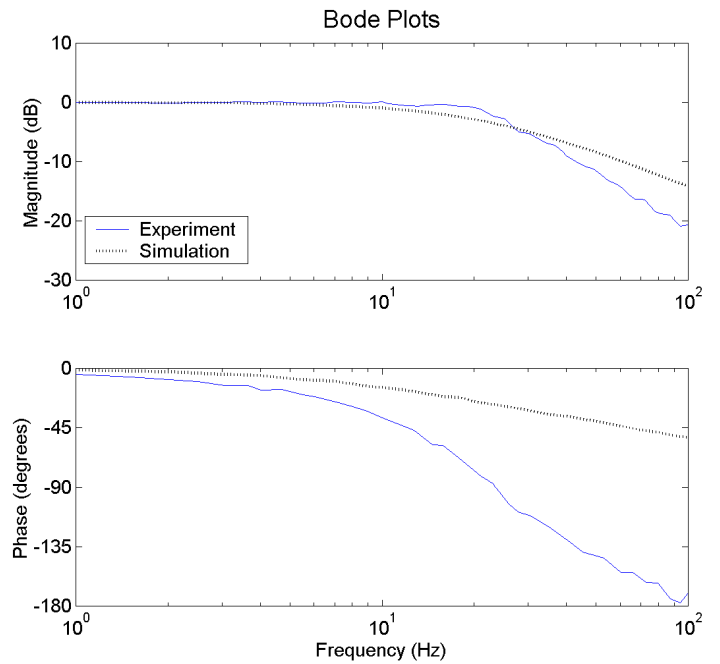


Figure 10, Frequency Response Curves